Earth Planet. Sci. Lett. 629 (2024) 118598

Contents lists available at ScienceDirect

Earth and Planetary Science Letters

journal homepage: www.elsevier.com/locate/epsl

Formation of lithium-rich pegmatites via rapid crystallization and shearing – case study from the South Tibetan Detachment, Himalaya

Xiao-Chi Liu [a,*], Matthew J. Kohn [b,*], Jia-Min Wang [a], Shao-Xiong He [a], Ru-Cheng Wang [c], Fu-Yuan Wu [a]

[a] State Key Laboratory of Lithospheric Evolution, Institute of Geology and Geophysics, Chinese Academy of Sciences, Beijing 100029, China
[b] Department of Geosciences, Boise State University, Boise, Idaho 83725, USA
[c] State Key Laboratory for Mineral Deposits Research, School of Earth and Engineering, Nanjing University, Nanjing 210023, China

ARTICLE INFO

Keywords:
lithium
rapid crystal growth
shearing
preferential extraction
South Tibetan Detachment System
Himalaya

ABSTRACT

Lithium is a key strategic metal with important reserves in pegmatites. However, the formation processes of Li-pegmatites remain doubtful, as most previous models are either qualitative or require large numbers of cyclic fractionation-extraction events that have little direct field evidence. Here, we propose that highly Li-enriched melts in the Himalaya may separate via an unusual combination of rapid crystal growth relative to diffusion of Li and water, and deformation in the context of the South Tibetan Detachment System (STDS). Models of boundary layer formation for felsic liquids show that rapid crystallization (1×10^{-7} to 1×10^{-8} m/s; c. 1 mm/day) of anhydrous minerals forms H_2O+Li-rich, mobile boundary layers, whereas H_2O+Li-poor, immobile boundary layers form adjacent to micas. Shearing can preferentially segregate inviscid, H_2O+Li-rich, boundary layers, producing extreme compositions and compositional gaps relative to parent magmas. The rock record of some magmas may not always reflect homogeneous liquid fractionation, rather preferential extraction of hydrous boundary layer liquids that develop adjacent to anhydrous minerals. This model explains whole-rock chemistry and field observations from the STDS, where Li-rich pegmatites and potential coeval source magmas occur with a distinct compositional gap. If our model is correct, the c. 2200 km-long STDS of Himalaya may represent an important zone of Li enrichment and site for future strategic Li-pegmatite reserves. Preferential extraction of boundary layers implies some evolved felsic magmas may not record crystallization of hydrous minerals.

1. Introduction

Lithium (Li) is a rare element of increasing economic importance. Although Li is enriched in upper continental crust, average concentrations are only 24 ppm (Rudnick and Gao, 2014), so economic viability requires geologic Li-concentrating processes. Pegmatites represent one of the main economic sources for lithium (Kesler et al., 2012; Ambrose and Kendall, 2020), with some deposits reaching weight percent levels and containing the rare minerals spodumene ($LiAlSi_2O_6$) and petalite ($LiAlSi_4O_{10}$). However, proposed processes by which Li concentrates in pegmatitic liquids to saturate Li minerals either have been qualitative (Rockhold et al., 1987; London, 1992; Webber et al., 1999; Maloney et al., 2008), or have required as many as 7 cyclic refining steps (Wu et al., 2020). Although fractional crystallization must play a role in concentrating Li, it is relatively compatible with micas, which are abundant in pegmatitic melts. A typical bulk distribution coefficient (K_d) between minerals and melt of ~0.5 for common granites implies inefficient Li accumulation in fractionating melts (Wu et al., 2020). How, then, can Li concentrate so effectively?

Here, we propose a mechanism for producing highly Li-enriched melts that appeals to a balance between the kinetics of crystal growth and diffusion of Li and water, coupled with deformation. Importantly, although the distribution coefficient (K_d) for Li between either mafic minerals or micas and melts ranges from mildly incompatible to compatible (0.2 to 1.7; Icenhower and London, 1995; Brenan et al., 1998), quartz and feldspar strongly exclude Li, leading to $K_d \leq 0.05$ (Maneta and Baker, 2014). For a specific balance between the rates of crystallization and diffusion, we show that crystallization of quartz, feldspar, and other anhydrous minerals will form inviscid boundary layers (melts) that are enriched in both water and Li. Formation of such boundary layers of unusual chemistry has been demonstrated experimentally for diverse melt compositions (e.g., Fenn, 1986; London et al.,

---

* Corresponding authors.
E-mail addresses: liuxiaochi@mail.iggcas.ac.cn (X.-C. Liu), mattkohn@boisestate.edu (M.J. Kohn).

https://doi.org/10.1016/j.epsl.2024.118598
Received 24 July 2023; Received in revised form 29 January 2024; Accepted 1 February 2024
Available online 13 February 2024

1989; Baker, 2005; Baker et al., 2008; London, 2014; Sirbescu et al., 2017). In contrast, our models show that crystallization of micas produces viscous boundary layers that are depleted in water and Li. Deformation may preferentially liberate the water-rich boundary layers adjacent to quartz and feldspars, leaving behind more viscous boundary layers adjacent to micas. This model quantifies a concept first presented theoretically (Tiller et al., 1953; Albarede and Bottinga, 1972), then qualitatively by many others (e.g., Jahns, 1982; Rockhold et al., 1987; London, 1992, 2014; Webber et al., 1999; Maloney et al., 2008), but accounts for local crystal effects and implicates deformation to extract melts effectively. Given the differences in K_d among minerals, the most effective melts for forming Li-rich pegmatites should be highly quartzo-feldspathic. Such parent liquids – leucogranites – are found worldwide, but are especially common in the Himalaya, in the uppermost Greater Himalayan Sequence, within and below the South Tibetan Detachment System (STDS) shear zone. In this study, we combine new and published data from Li-pegmatites near Mount Qomolangma (Everest; Fig. 1) and local associated but less Li-enriched granites to show how our model can explain formation of these unusual strategic deposits in the context of crystallization processes, regional geology, and tectonics.

2. Geologic setting of Himalayan leucogranites and pegmatites

The Himalayan orogen represents a principal expression of the collision between India and Asia (Fig. 1), and leucogranites and pegmatites are widespread along its entire strike length of c. 2200 km. Intrusions are concentrated towards the top of the Greater Himalayan Sequence (GHS), which represents the exhumed, high-grade, metamorphic core of the orogen (Kohn, 2014; Searle et al., 2009; Yin, 2006). Structurally, the GHS is bounded above by the normal-sense STDS and Tethyan Himalayan Sequence (THS) (Weinberg, 2016; Yin, 2006). Partial melting of the GHS to form leucogranitic melts initiated at 40-45 Ma (Ding et al., 2021), whereas most melt segregation and crystallization spanned ~25 to ~15 Ma (Searle et al., 2009; Weinberg, 2016). Melt extraction and crystallization broadly correspond with STDS movement (Searle et al., 2009; Yin, 2006), pointing to a change in either the mechanical strength of the upper crust or boundary forces at that time (Burchfiel et al., 1992; Dahlen, 1990). Very generally, STDS extension during melt intrusion thinned the crust, causing collapse of the Himalayan overthickened crust (Burchfiel et al., 1992).

Two specific geographic areas associated with the STDS are considered here. The Pusi La region (Fig. 1B) hosts abundant Li-pegmatites (Liu et al., 2020; Qin et al., 2021), but exposure is relatively poor, and the local transect imperfectly constrains the relationships to other igneous bodies and the STDS. Farther north, the local Ra Chu transect traverses a prominent ridgeline and includes a ca. 30 m-thick cliff exposure of the uppermost section of the STDS shear zone (Figs. 1-2). The outcrop consists largely of basal calc-silicate rocks (North Col Formation) and overlying marbles (Yellow Band), which together represent the Rouqiecun Group (uppermost GHS; Fig. 2A-E; Jessup and Cottle, 2010). The calc-silicate rocks are mainly intruded by foliated leucogranites (Fig. 2F-H) that present as lenses concordant with the prominent mylonitic fabric in the outcrop, whereas overlying marbles are intruded by foliated pegmatite pods (Fig. 2C-E). In both the Pusi La and Ra Chu regions, the lower part of the North Col Formation is intensely intruded by leucogranite sheets (Fig. 2G), similar to exposures to the south and east of Cho Oyu (8201 m) and along the Rongbuk Valley (Chaya, Rongbuk, Hermit's Gorge; Fig. 1) (Cottle et al., 2011).

3. Methods

3.1. Field collections

Leucogranite and pegmatite samples were collected from previously published sections at Pusi La (Liu et al., 2020) and from the newly discovered Ra Chu transect (Figs. 1-2). We investigated 65 samples between ~28.0°N and ~28.4°N along the northwest side of Mount Qomolangma for whole-rock geochemistry. All of the samples are in Greater Himalayan Sequence rocks in the footwall of the STD shear zone. The footwall has experienced substantial top-to-the-north shearing but is lithostratigraphically and metamorphically distinct from the overlying Tethyan Himalayan Sequence. The spodumene-bearing pegmatites spread heterogeneously over a north-south distance of more than 30 km. At Ra Chu, these spodumene-bearing pegmatites occur as lenses, 0.5~3 m long and 0.2~1.5 m wide (Fig. 2C-E). The leucogranites contain a typical magmatic mineral assemblage of K-feldspar, quartz, plagioclase, muscovite, biotite, garnet, and tourmaline, with accessory beryl, monazite, zircon, and apatite. The Li-rich pegmatites contain coarse early spodumene with finer-grained quartz, K-feldspar, and plagioclase (Fig. 3A-F), late petalite (Fig. 3G-H), and accessory tourmaline, beryl, cassiterite, members of the columbite group, monazite, zircon, and apatite.

3.2. Whole-rock analysis

Whole-rock analyses were collected as described in Liu et al. (2020). Large samples were first crushed and split. Major element compositions were determined by Zsx Primus II wavelength dispersive X-ray fluorescence spectrometer (XRF) according to Chinese National standard protocol GB/T 14506-2010DZG93-05 at the China National Nuclear Corporation, Changsha, China. The relative standard deviation (±2σ) is less than ±5%. Trace element analysis of whole-rock was conducted on Agilent 7700e ICP-MS at the Wuhan Sample Solution Analytical Technology Co., Ltd., Wuhan, China. For trace element compositions, 100 mg of powder were digested in a mixture of 1 ml concentrated HF and 0.5 ml concentrated HNO_3 in PTFE-lined stainless-steel bombs at 190°C for 72 hours. Any residues were dissolved in 8 ml of 40 vol% HNO_3 at 110°C for 3 hours. Standard reference materials (USGS standards BHVO-2, AGV-2, and W-2, and GeoPT9 standard OU-6) were used for calibration. Precision for trace element concentrations is better than ±10% relative (±2σ). Raw data are provided in Supplemental Table S1; median compositions and calculated viscosities for comparison with model properties are provided in Supplemental Table S2.

3.3. Modeling boundary layer concentrations

Models of boundary layer concentration profiles (Table S3) were constructed using expressions from Tiller et al. (1953). For a crystal-liquid interface moving at velocity v, a steady-state composition profile develops adjacent to crystals of form:

$$C_i(x) = C_{i,init} + C_{i,init}\left(\frac{1}{K_d} - 1\right)e^{-vx/D_i} \tag{1}$$

where $C_{i,init}$ is the initial concentration of the element i in the (parent) liquid, K_d is the distribution coefficient between crystal and liquid (i.e., $C_{i,crystal}/C_{i,liquid}$), x is distance into the liquid from the crystal-liquid interface, and D_i is the diffusion coefficient for element i in the liquid. Tiller et al. (1953), Albarede and Bottinga (1972), Kohn and Penniston-Dorland (2017), and Phelps et al. (2020) illustrate how such profiles develop, while others document experimentally the formation of boundary layers that are chemically distinct from bulk liquid (e.g., Fenn, 1986; London et al., 1989; Baker et al., 2005; Baker, 2008; London, 2014; Sirbescu et al., 2017). Generally speaking, these boundary layers are melts, but of a different chemistry and viscosity from bulk liquid. Our model expands concepts presented in Tiller et al. (1953), Albarede and Bottinga (1972), and later pegmatite researchers (e.g., Jahns, 1982; Rockhold et al., 1987; London, 1992, 2014; Webber et al., 1999) to evaluate quantitatively how local crystal growth rates and deformation might combine to produce and extract Li-enriched melts effectively. Conceptually, we initiate models with a liquid of specified Li

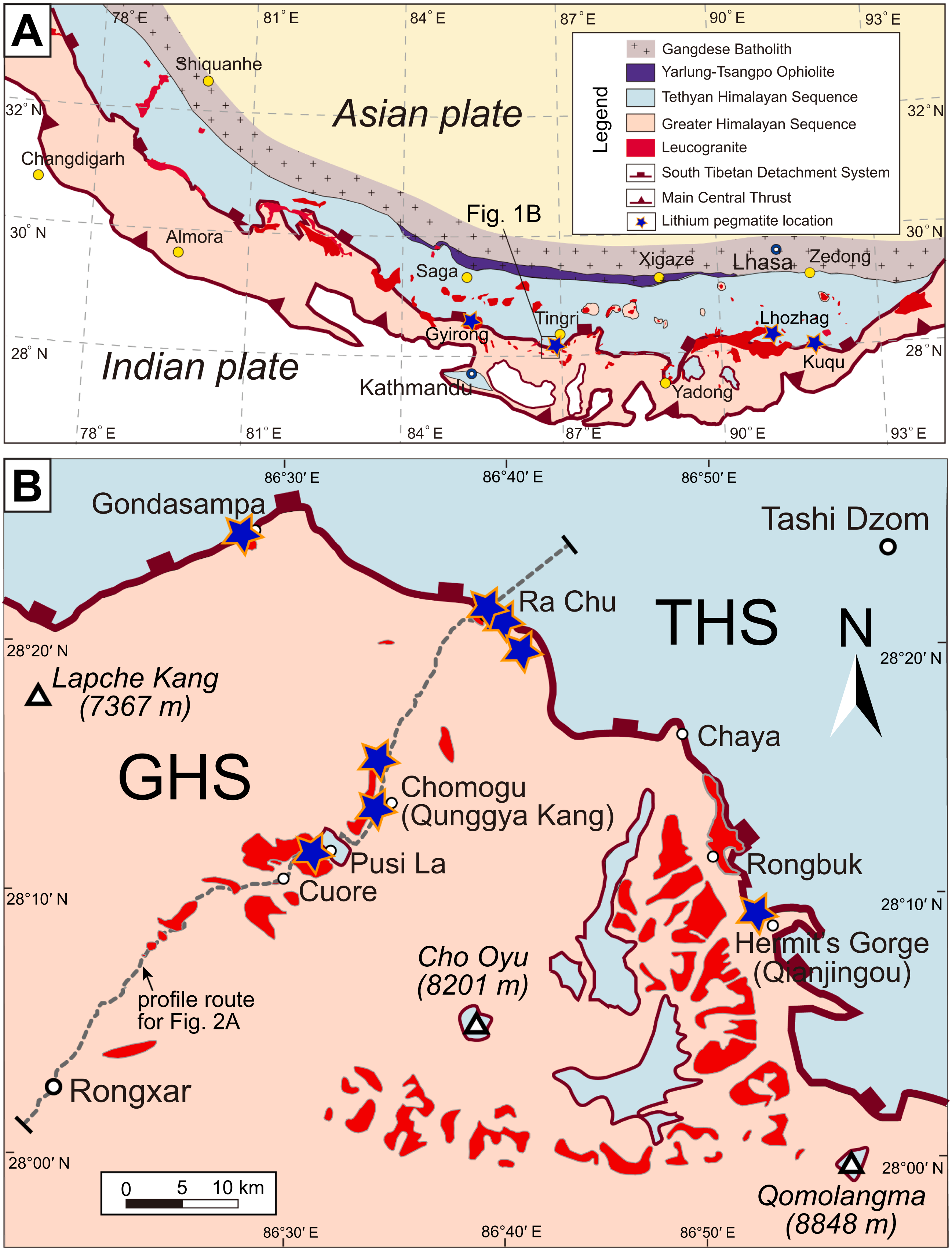

Fig. 1. (A) Simplified geological map of the Himalayan orogen (Modified from Wu et al. (2020)). Pegmatites (stars) occur along the South Tibetan Detachment System, which separates the structurally higher Tethyan Himalayan Sequence from the structurally lower Greater Himalayan Sequence. (B) Simplified geological map of Mount Qomolangma (Everest) region (modified from Liu et al. (2020)). Pegmatites (stars) occur just below Tethyan rocks, within the South Tibetan Detachment System shear zone and in close association with leucogranites.

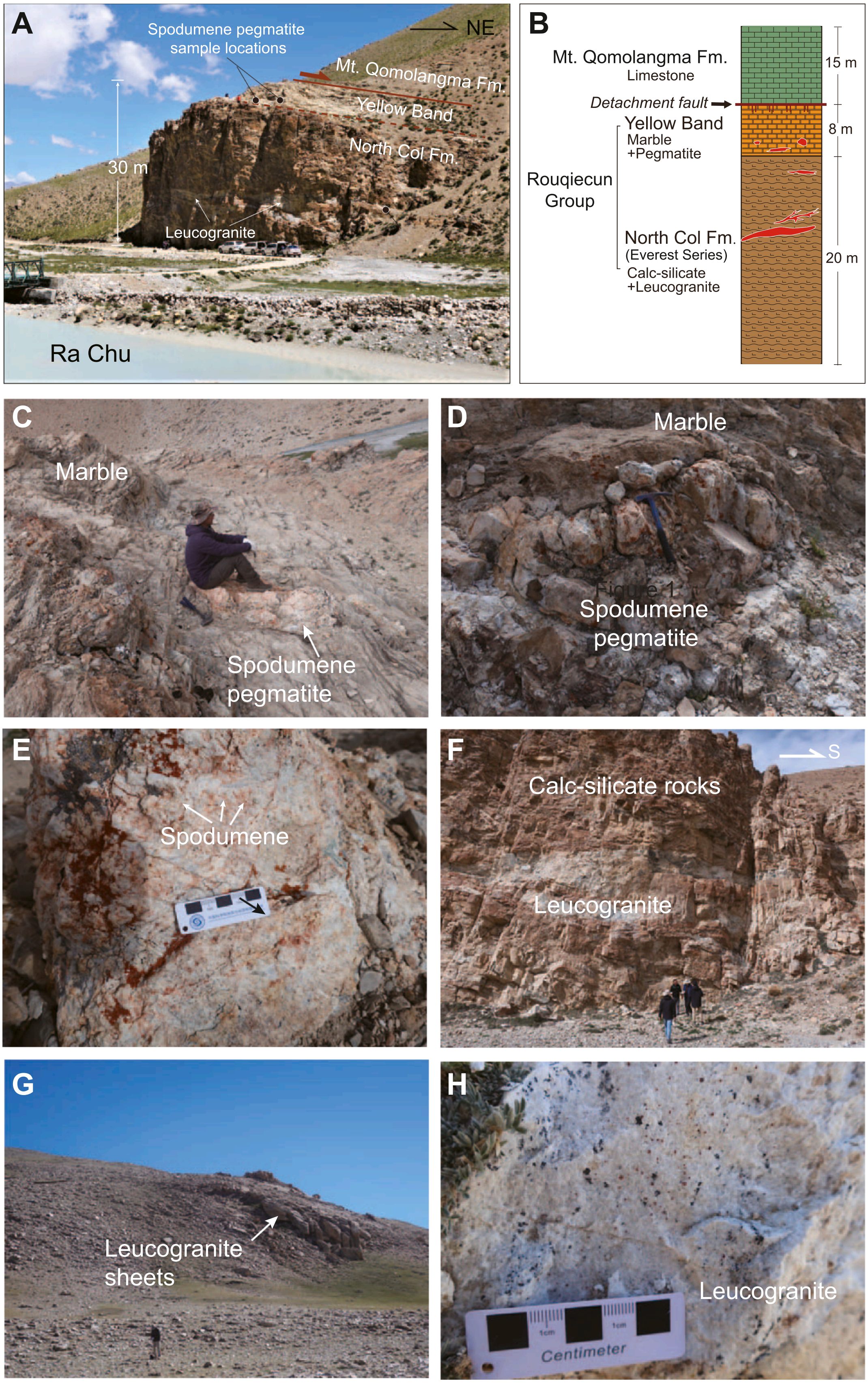

Fig. 2. Field occurrences of pegmatite and leucogranite from the Ra Chu transect showing associations and scales. (A) Outcrop at Ra Chu showing distribution of rock types. (B) Simplified stratigraphic section, showing concentration of leucogranites and pegmatites in the uppermost GHS; pegmatites occur in the Yellow Band marble. (C-E) Pegmatites with cm-scale spodumene are associated with marbles and calc-silicates of the Rouqiecun Group (uppermost Greater Himalayan Sequence). (E-H) Leucogranites intrude as sheets and are nearly devoid of mafic minerals excepting tourmaline.

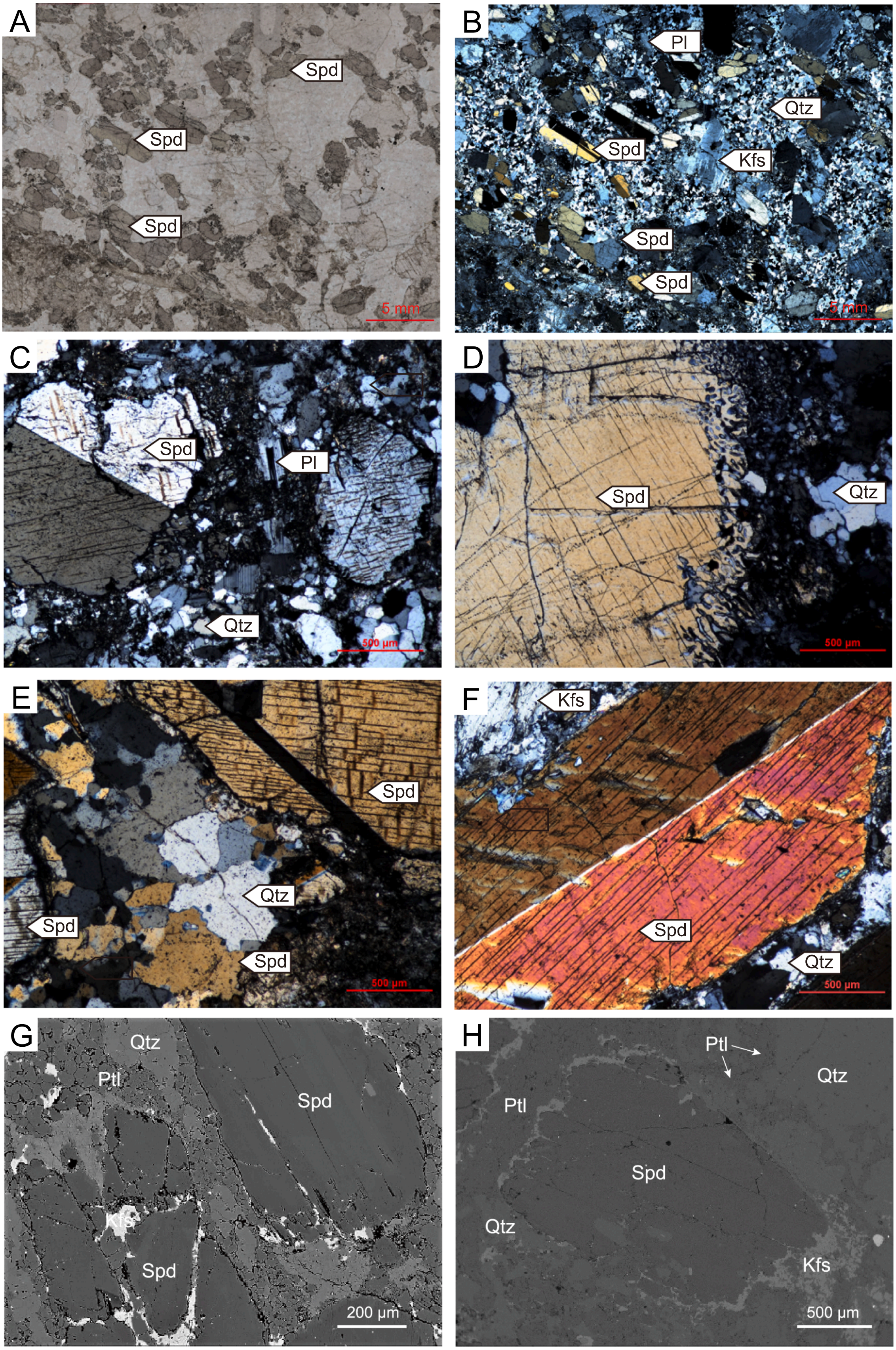

Fig. 3. Images of representative mineral textures in pegmatites from the Ra Chu transect. (A-F) Photomicrographs show undeformed coarse spodumene in fine-grained groundmass of quartz and feldspar. (G-H) Backscattered electron images show K-feldspar and petalite developed around the edges of spodumene phenocrysts. Pl-plagioclase; Kfs-K-feldspar; Qtz-Quartz; Ms-Muscovite; Ptl-petalite; Spd-Spodumene.

concentration, fractionally crystallize it to create a crystal mush, input crystal growth rates, assume temperature and calculate diffusion and viscosity profiles adjacent to crystals, then evaluate potential mobility of different boundary layers for that growth rate. Calculations are then repeated for different assumed growth rates. We make no attempt to model evolution of extracted liquids, however, and further enrichment and zonation of crystallizing Li-rich liquids are both possible.

For the first step in this calculation (fractional crystallization of an initial melt), we assumed Li and H_2O concentrations in felsic liquid of 150 ppm (μg/g; well within the range of granites in the region; Table S1, section 4.1) and 2 wt% that undergoes fractional crystallization of 75%. This initial liquid could have been derived from partial melting of GHS either down-dip to the north or from structurally lower rocks in the study area. The water content is higher than measured in whole rocks, but accounts for loss of H_2O via escape of water-rich boundary layers (e.g., our model) or an aqueous phase during final crystallization. A bulk K_d for modeling initial fractional crystallization was determined by proportioning mineral-specific K_d's and assuming proportions of crystallizing minerals. We assumed $K_d = 0.05$ for quartz and feldspar (Jolliff et al., 1992; Zajacz et al., 2009; Maneta and Baker, 2014) and 1.5 for micas (Icenhower and London, 1995). For mineral-specific H_2O partitioning, we assumed that micas take up ~5 wt% H_2O (so $K_d = 2.5$), and that the maximum concentration of H_2O adjacent to quartz and feldspar is 10 wt% (so $K_d = 0.2$) (Holtz et al., 2001). Although quartz and feldspar are nominally anhydrous (implying $K_d \sim 0$), they will contain some hydrogen plus liquid inclusions (implying $K_d > 0$). We then assumed initial fractionation with mineral proportions of 30% biotite and/or muscovite, and 70% plagioclase, K-feldspar, and quartz, yielding a bulk $K_d = 0.5$ for Li and 1.0 for H_2O. These values lead to concentrations ($C_{i,init}$) in interstitial melt (after 75% crystallization) of 300 ppm Li and 2 wt% H_2O. Less crystallization of micas would lead to lower bulk K_d and higher Li concentrations. We do not model phase separation of an aqueous phase, but compositional implications of this process are discussed in detail in section 4.4.

Application of Equation 1 requires values for D_{Li} and D_{H2O}. We assumed temperature- and composition-dependent D's for Li in rhyolite (Zhang et al., 2010) and H_2O in peraluminous rhyolite (Zhang and Ni, 2010) at 5 kbar and an average 6 wt% H_2O adjacent to feldspar (for K_d =0.2, profiles range from 2 to 10 wt%, so the average is ~6 wt%) and 1 wt% adjacent to mica (for $K_d = 2.5$, profiles range from 0.8 to 2 wt%). Use of a single average H_2O content permits analytical solutions and is accurate to within a factor of 5. This approximation does slightly underestimate vs. overestimate boundary layer thicknesses adjacent to feldspar vs. mica and the shape of the profile (true profiles will be slightly "flatter" adjacent to feldspar and slightly "thinner" adjacent to mica).

The size and shape of boundary layer profiles depend on specific values of K_d, D, and v. Enrichments and depletions scale inversely with K_d, and a factor of 2 decrease in K_d for Li in feldspar and quartz (0.025 rather than 0.05) would lead to greater enrichments by a factor of 2. A lower K_d for H_2O in quartz and feldspar would likely lead to aqueous phase separation. If this phase is not saline, it will not be enriched in Li (Webster et al., 1989) and will not affect our calculations. Further implications of aqueous phases and salinities are discussed in section 4.4. Crystal growth velocity scales equivalently with D, so an increase in D by a factor of 2 would require an equivalent increase in crystal growth velocity to produce the same profile.

3.4. Modeling viscosities

Viscosities were calculated (Table S3) according to the model of Giordano et al. (2008) for hydrous melt with a major element composition corresponding to the median muscovite leucogranite in the Ra Chu and Pusi La transects. Use of other local bulk-rock compositions (two-mica granite, tourmaline leucogranite, etc.) do not affect our conclusions. The model of Giordano et al. (2008) accounts for complex melt chemistry, but rather than calculate all possible melt chemistries adjacent to all possible crystals (which would require solving Equation 1, accounting for major element partition coefficients for all minerals and diffusion rates for all elements), we simply assumed a fixed major element composition and adjusted H_2O and Li contents. This calculation may overestimate viscosities adjacent to Si-rich minerals, and underestimate viscosities adjacent to some Si-poor minerals, but suffices for illustration. Although the model of Giordano et al. (2008) does not explicitly account for the effects of Li on melt viscosity, increasing mole fractions of all alkali metals affects melt viscosity similarly (Fig. 4 of Hess et al.1995). We found that simply lumping the molar proportions of Na and Li as "Na" in the model of Giordano et al. (2008) reproduces measured $\log_{10}$ viscosities from Hess et al. (1995) to within ~0.5 for Li contents up to 5 wt% Li_2O. Computationally, viscosities for the muscovite leucogranite can be accurately calculated by modifying a simple expression from Hess and Dingwell (1996) for haplogranite. At 700°C (likely magmatic temperature; Wu et al., 2020) this expression is:

$$log_{10}(\eta, G\ et\ al.) = 0.963 \cdot log_{10}(\eta,\ H\&D) - 0.135 \cdot H_2O(wt\%) - \frac{Li(ppm)}{1000}(0.147 - 0.060 \cdot H_2O(wt\%)) + 0.86 \tag{2}$$

where "η,G et al." is the viscosity as calculated using the complex expression of Giordano et al. (2008) adjusted for Li content and "η,H&D" is the viscosity as calculated using the simple expression of Hess and Dingwell (1996). The analogous expression at 500°C (likely wall-rock temperature; Cottle et al., 2011) is:

$$log_{10}(\eta, G\ et\ al.) = 1.139 \cdot log_{10}(\eta,\ H\&D) - 0.085 \cdot H_2O(wt\%) - \frac{Li(ppm)}{1000}(0.2296 - 0.0673 \cdot H_2O(wt\%)) - 1.08 \tag{3}$$

Equations 2 and 3 are simple to implement and reproduce calculated $\log_{10}$ viscosities of Giordano et al. (2008) to within 0.1. We did not attempt to account for F contents, which regionally range from ~50 ppm to ~1 wt%. Fluorine contents of 0.5 wt% would reduce $\log_{10}$ viscosity by 0.2 to 0.3.

3.5. Calculating bounds on pressure gradients and differential stresses

Pressure gradients needed to drive Poiseuille flow along a planar sheet can be calculated from assumed flow rates and boundary-layer liquid thicknesses and viscosities:

$$\frac{-dP}{dz} = \overline{v}(z) \cdot \frac{12\eta}{l^2} \tag{4}$$

where dP/dz and $\overline{v}(z)$ are the pressure gradient and mean velocity in the z-direction, η is viscosity, and l is the half-thickness of the sheet. The key to solving Eq. 4 is that we must identify bounds on $\overline{v}(z)$ and l. For $\overline{v}(z)$, flow must transport Li faster than diffusion, or diffusion will homogenize compositions. Using Li diffusivity from Zhang et al. (2010), the characteristic diffusion distance [$=2(Dt)^{½}$] per year for Li is ~6 cm at 700°C, so $\overline{v}(z) > \sim 6$ cm/yr. For l, because Himalayan leucogranites typically have grain sizes of mm's (Scaillet and Searle, 2006), interstitial residual melts must have similar or thinner total thicknesses (mm's or smaller). Boundary layers are only a small fraction of total melt thickness, implying e-folding distances <<1 mm. Spatial scales of boundary layers depend on crystallization rate (faster crystallization forms thinner layers), and our calculations show that H_2O-rich boundary layers form on spatial scales less than 1 mm only for crystallization rates greater than 1×10^{-8} m/s (see section 4.2). These constraints of ($\overline{v}(z) > \sim 6$ cm/yr and crystallization rates $> 1 \times 10^{-8}$ m/s) allow solution of Equation 4 for $\frac{-dP}{dz}$ vs. distance ($=2l$) from the crystal-liquid interface.

Using Equation 4, pressure gradients needed to drive flow at $\overline{v}(z)=6$ cm/yr were calculated, numerically integrating viscosities across variable distances, l, from the crystal-liquid interface (Table S3). Pressure

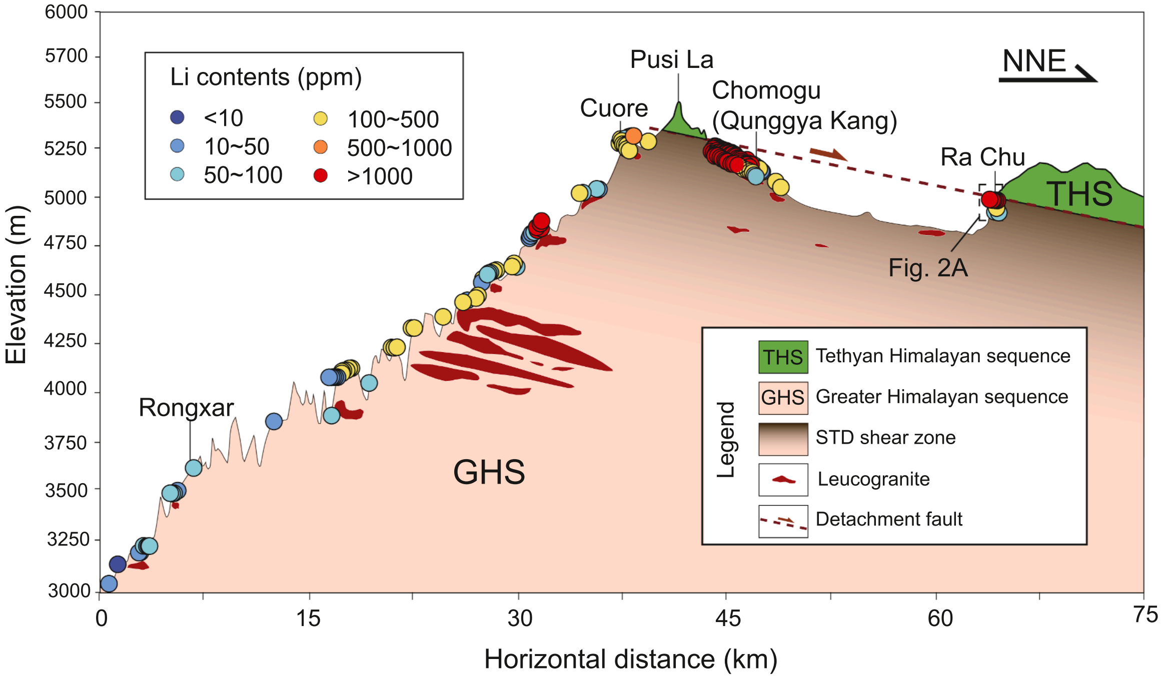

Fig. 4. Lithium concentrations for felsic intrusions near Mt Qomolangma (Everest), southern China, along elevation profile from Rongxar in the southwest across Pusi La to Ra Chu in the northeast (see Fig. 1B for locations). THS = Tethyan Himalayan Sequence; GHS = Greater Himalayan Sequence.

gradients are infinite at the crystal-liquid interface, regardless of what is crystallizing, because viscosity is finite, but l=0. To transport melts adjacent to anhydrous minerals, pressure gradients first decrease with increasing l to a minimum that represents maximum melt mobility. This minimum value balances low melt viscosity close to crystal surfaces with moderate boundary layer thickness. Calculated pressure gradients then increase to a maximum as viscosity increases into the melt, then decrease gradually as integrated viscosity approaches background melt viscosity and l increases. For melts adjacent to micas, calculated pressure gradients monotonically decrease as viscosity decreases away from the crystal surface while l increases.

For calculating the maximum lithostatic-magmatic pressure gradient differences, we assumed densities of 2.75 g/cm^3 for solid rock (typical for upper crust) and 2.20 g/cm^3 for pegmatite melt with 6 wt% water (see Supplemental Table S2). The latter calculation used the method of Bottinga (1970) with volume, thermal expansion, and compressibility data from Kress and Carmichael (1991), Lange (1994), and Lange and Carmichael (1987).

Calculation of differential stress needed to drive flow through a fracture is based on Equation 8 of Rubin (1995), divided by 4 for accuracy (see Rubin, 1995, for discussion):

$$v = \frac{l(\Delta\sigma)^3}{12\eta M^2} \tag{5}$$

where v is velocity, Δσ is differential stress (overpressure), M is elastic stiffness (40 GPa for granite at 5 kbar and 500-700°C (Hacker and Abers, 2004)), and l is fracture length, here taken as 1 mm (minimum grain size). This equation neglects factors such as surface tension, so calculates a maximum velocity.

4. Results and discussion

4.1. Extreme lithium enrichment within the STD shear zone

Lithium concentrations of the samples range from ~10 ppm to ~14000 ppm, with key differences emerging depending on rock type and structural position (which correlate; Fig. 4; data in Supplemental Table S1 include elevation). At lower structural levels (2963 to 3965 m elevation at Pusi La; 4825 to 4840 m elevation at Ra Chu), biotite granite and tourmaline leucogranite dominate, with low median Li concentrations of ~50 ppm (Fig. 4; Table S1). Intermediate structural levels at Pusi La (4340 to 4475 m) mainly contain two-mica granite with moderate median Li concentrations of ~140 ppm (Fig. 4). A pegmatite zone occurs at high structural levels (4624 to 4794 m at Pusi La; 4849 m at Ra Chu), with extremely high median Li concentrations of ~5100 ppm (Pusi La) and ~6300 ppm (Ra Chu; Fig. 4). The highest structural levels (4853 to 5364 m at Pusi La; 4974 to 4990 m at Ra Chu) contain a wide variety of magma types (tourmaline leucogranite, two-mica granite, muscovite-leucogranite, and pegmatite) with moderate median Li concentrations of ~180 ppm (Pusi La) and ~170 ppm (Ra Chu). Focusing on the new Ra Chu ridge transect, most spodumene pegmatites concentrate at the structurally high boundary between the “Yellow Band” marble and North Col Formation calc-silicate rocks (Fig. 2B). The Li contents of these Li-enriched pegmatites mostly range from ~2500 to ~14000 ppm (Fig. 5). In contrast, most leucogranites and related pegmatites within the lower part of the footwall of the STD shear zone have low Li contents of ~40 to ~200 ppm (Figs. 4-5). Concentrations of Li and Sn correlate positively (Fig. 5A), while Li and Zr/Hf correlate inversely (Fig. 5B), forming distinct clusters of data with a distinct gap separating high- and low-Li magmas. Chondrite normalized rare earth element (REE) patterns from spodumene pegmatites show flat REE patterns with concave tetrads and no Eu anomaly (Fig. 5C).

Field, petrographic, geochemical, and geochronological data suggest the leucogranites and pegmatites from the Pusi La section are contemporaneous and cogenetic, such that nearby granites are the most probable parental magma for the more chemically-evolved, rare metal-rich pegmatites (Liu et al., 2020). The close spatial association between synkinematic spodumene pegmatites and crustal-scale transcurrent shear zones further suggests a causative link between the two. The emerging question from these observations is: What controls the extreme enrichment of Li? As discussed next, our calculations suggest boundary layers that form on rapidly growing crystals may be responsible.

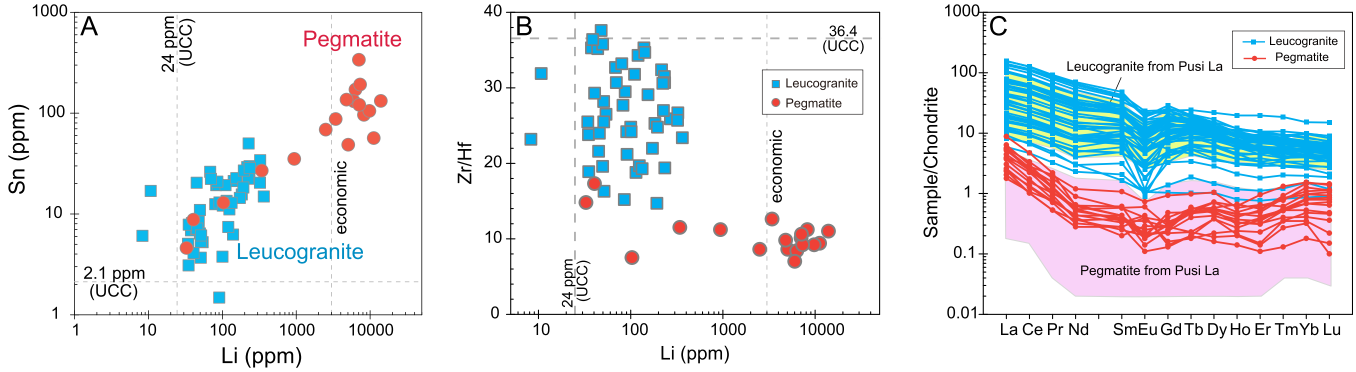

Fig. 5. Whole-rock trace element compositions from the Ra Chu and Pusi La sections. (A, B) Sn and Zr/Hf versus Li, showing clusters of data with large compositional gaps between leucogranites and pegmatites. Most economic deposits have Li >~3000 ppm. Data for Pusi La are from Liu et al. (2020). (C) Rare earth element patterns, showing generally low concentrations in pegmatites. UCC=average concentration for upper continental crust (Rudnick and Gao, 2014).

4.2. A quantitative model for extreme Li enrichment

Differentiation of magmas to form Li-rich boundary layers that are both extractable (inviscid) and thinner than typical crystal sizes in granites (Scaillet and Searle, 2006) requires a balance between rapid crystallization and relatively high temperature. At a likely magma temperature of ~700°C (Wu et al., 2020), our models show that growth rates of 1×10^{-7} to 1×10^{-8} m/s (c. 1 mm/day) form boundary layers on scales <1 mm (Fig. 6A, B), squarely within the range of growth rate estimates for magmatic phenocrysts (1×10^{-6} to 1×10^{-9} m/s) (Webber et al., 1999; data from Sirbescu et al., 2008; Phelps et al., 2020; Zhang and Lee, 2021). Lower growth rates and temperatures can also yield boundary layers ≤~1 mm, e.g., 2×10^{-9} m/s at 500°C (a likely wallrock temperature) (Cottle et al., 2011). However, viscosities are 2-4 orders of

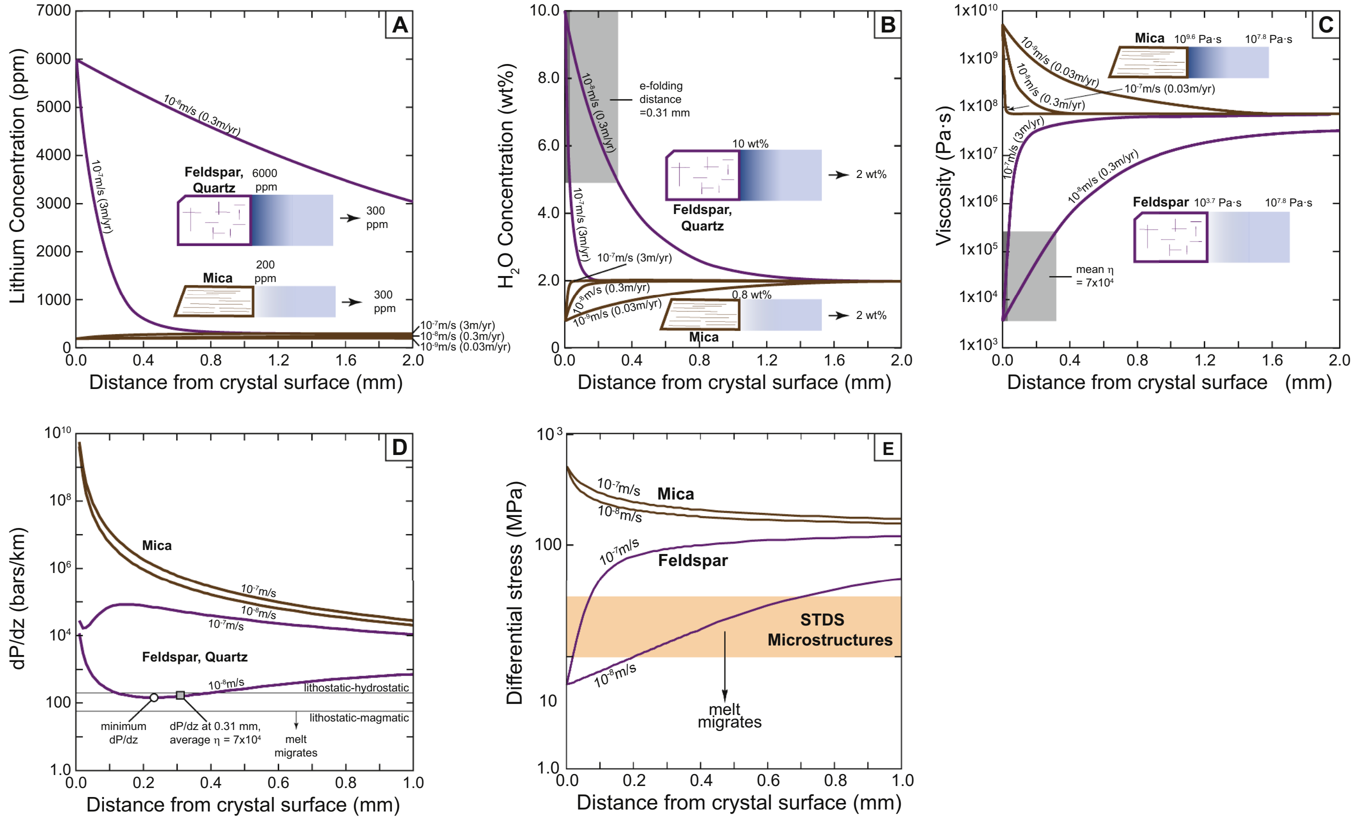

Fig. 6. Models of Li concentration, water concentration, viscosity, and pressure gradient needed for transport at 6 cm/yr at 700°C. Insets schematically show Li concentrations, H_2O concentrations, and viscosity profiles developed in melt adjacent to quartz, feldspar, and mica; darker blue indicates higher concentration or viscosity. (A and B) Lithium and H_2O concentration vs. distance. Boundary layer adjacent to quartz and feldspar is highly Li– and H_2O–enriched, while layer adjacent to mica is Li– and H_2O–depleted. Gray areas bound water contents for e-folding distances corresponding with crystallization rates of 10^{-8} to 10^{-7} m/s. (C) Viscosity vs. distance. H_2O-poor boundary layer adjacent to mica is highly viscous. H_2O-rich boundary layer adjacent to quartz and feldspar (and other anhydrous minerals) is inviscid. Gray regions correspond with e-folding distances from (B) and have average $\eta = 7\times10^4$ Pa·s. (D) Calculated pressure gradient vs. distance from the crystal-liquid interface. Gray square shows calculation at e-folding distance for crystallization rate of 10^{-8} m/s. Calculated minimum (white dot at ~150 bars/km and ~0.22 mm) occurs adjacent to anhydrous minerals with moderate crystallization rates (10^{-8} m/s). Adjacent to micas, calculated pressure gradients are too high (melts are too viscous) for flow to occur. (E) Calculated differential stress vs. distance from crystal surface. Differential stresses calculated from microstructures within the STDS are sufficient to mobilize boundary layers adjacent to quartz and feldspar but not micas.

magnitude higher (Tables S2-S3), making these boundary layers harder to segregate. In contrast to anhydrous minerals, crystallization of micas does not form Li-enriched boundary layers (Fig. 6A) because micas take up too much Li (K_d is too high).

Viscosity depends strongly on water content (Giordano et al., 2008), so exclusion of water adjacent to crystallizing anhydrous minerals (K_d<<1) creates boundary layers that are relatively water-rich (Fig. 6B) and inviscid (Fig. 6C) – we show results for quartz and feldspar, but for these simplistic models the same principle applies to all anhydrous minerals, including monazite, oxides, zircon, etc. Viscosities $<\sim1\times10^5$ Pa·s at 700°C (Fig. 6C) promote extraction. In contrast, preferential uptake of water adjacent to micas (Fig. 6B; K_d=2.5) creates a highly viscous (4×10^9 Pa·s at 700°C; Fig. 6C; 4×10^{13} Pa·s at 500°C; Tables S2-S3), less extractable layer. That is, anhydrous minerals form boundary layers that are both H_2O-rich (inviscid, extractable) and highly enriched in Li (Fig. 6A-C), while micas develop boundary layers that are H_2O-poor (viscous, non-extractable) and Li-depleted. Extraction of the inviscid layers adjacent to anhydrous minerals could occur, leaving viscous layers adjacent to hydrous minerals behind.

How and when are the inviscid layers extracted? Bulk magma crystal contents must be ≥70%, otherwise convection can destroy boundary layers (Bachmann and Bergantz, 2008). Melt viscosities are also generally too high for density-driven segregation (McKenzie, 1985), and segregation via shearing is too slow (Scaillet and Searle, 2006). Instead, high local pressure gradients in the context of shearing appear necessary. Minimum pressure gradients for melt segregation can be calculated subject to constraints that flow must transport Li faster than diffusion (~6 cm/yr at 700°C) and boundary layers must be <1 mm thick (crystallization rates $>1\times10^{-8}$ m/s).

Pressure gradients needed to mobilize melt are unrealistically high adjacent to micas (100s of kbar/km), indicating these boundary layer melts are immobile. Adjacent to anhydrous minerals, pressure gradients needed to mobilize melt may be as low as ~150 bars/km (Fig. 6D), but this is still too high for hydrous melt to escape boundary layers by lithostatic vs. magmatic pressure gradients alone (c. 50 bars/km) on timescales sufficiently short to prevent Li homogenization. Formation of a Li-enriched aqueous phase (Ellis et al., 2022; Fan et al., 2020), although not supported experimentally unless extremely saline (Webster et al., 1989; see section 4.3), would readily separate by lithostatic vs. aqueous pressure gradients alone. Assuming Li partitions into hydrous melt (and not into aqueous fluid), tectonic context provides a simple explanation for melt extraction. Shearing of mechanically heterogeneous materials in the context of local differential stresses can mobilize melt (Rubin, 1995; Rutter and Neumann, 1995). Microstructural measurements indicate differential stress in the STDS ranged from 10 to 35 MPa (Law et al., 2011), which is capable of mobilizing boundary layers adjacent to quartz and feldspars, although not adjacent to micas (Fig. 6E). Shearing along the STDS during melt crystallization logically squeezes hydrous boundary layers adjacent to anhydrous minerals into larger pockets and layers. Once melt has segregated into horizons thicker than a few mm's, the difference between lithostatic and magmatic pressure gradients becomes sufficient to drive melts upward along fractures or other structural weaknesses to form higher-level pegmatites. Thus, high differential stresses need not be imposed on boundary layers for long periods of time, only until they have migrated sufficiently (cm's) to form larger pockets.

The STDS meets all three conditions for our model to form Li-pegmatites (Fig. 7):

1. Leucogranites intruded relatively cold wall rocks (Fig. 7A), so that heat loss and crystallization were rapid, forming chemical boundary layers (Fig. 7B)
2. Relatively high crystallization temperatures (c. 700°C) promoted low melt viscosity.
3. Transient differential stresses >~10 MPa during deformation promoted extraction of H_2O-rich boundary layers (Figs. 6D, 7B, C).

4.3. *Comparison to other Li-enrichment models*

Many processes have been proposed to explain compositionally-extreme liquids, but trace melting of a highly-enriched source (Grew, 1998), extreme fractional crystallization (Černý et al., 2012), or repeated fractional crystallization coupled with melt segregation should produce continuous ranges in composition (Wu et al., 2020), which we do not see. For example, Li concentrations show a distinct gap of Li ≤ ~300 ppm (leucogranites) vs. Li ≥ ~3000 ppm (pegmatites; Fig. 5A, B). Constitutional zone refinement (passage of a melt zone through a solid) purifies the solid but cannot produce extreme trace element enrichment in the liquid (Tiller et al., 1953). Thus, these mechanisms do not appear generally viable.

In principle, an immiscible aqueous phase could form and separate during late stages of magma crystallization, depending on assumed K_d for H_2O and water content of the initial melt (e.g., London, 2014; Sirbescu et al., 2017). If the aqueous phase has NaCl contents <~5 wt%, it

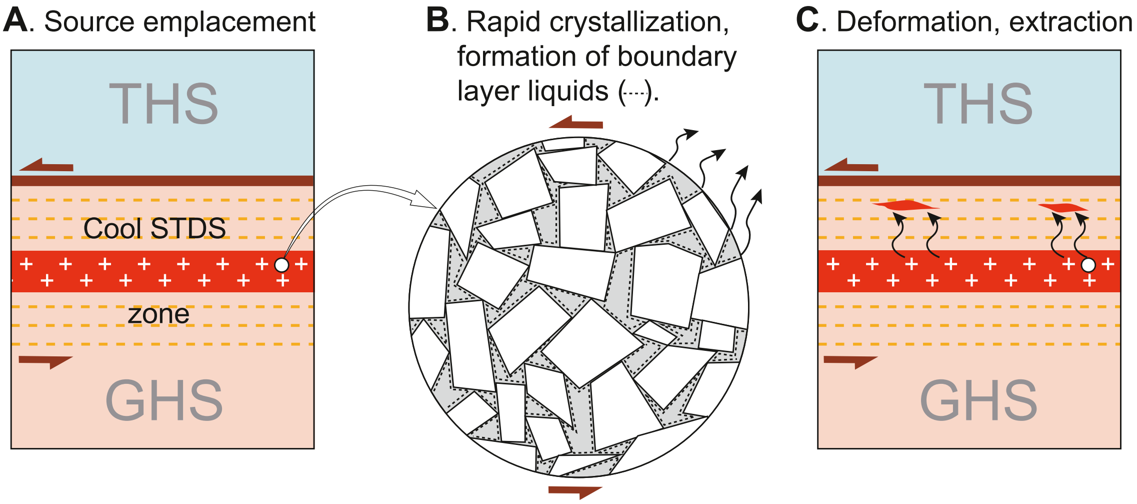

Fig. 7. Schematic drawing (not to scale) of processes leading to Li-enriched pegmatites in the top of the STDS shear zone. (A) Leucogranites (red) derived from partial melting of the GHS at depth intrude as sills into the STDS zone. (B) Fractional crystallization leads to mechanical lockup and formation of boundary-layer liquids, enriched in Li and H_2O (see Fig. 3) and potentially capable of exiting the system (curvy arrows). (C) Deformation creates transient pressure gradients that preferentially extract inviscid boundary layers.

will not concentrate Li preferentially compared to melt (Webster et al., 1989), so would not be effective for forming Li-pegmatites. Only when salinities exceed 11 wt% can aqueous solutions preferentially concentrate Li (Webster et al., 1989; Zajacz et al., 2008). Although fluid inclusions have not been investigated in the studied Li-rich pegmatites, we are unaware of evidence for such a salty aqueous phase in similar pegmatites elsewhere. Further arguing against this mechanism, high CO_2 contents from decarbonation of surrounding carbonates and calc-silicates would decrease maximum salinity (Bowers and Helgeson, 1983) and Li.

A recent model invokes two partial melting events of Li-enriched micaceous rocks to create Li-rich melts (Koopmans et al., 2023). The first melting event requires separation of small volume (<10%) melt with c. 500 ppm Li. Complete crystallization of this magma, followed by partial remelting and separation of another small volume (<10%) melt could enrich Li to several thousand ppm. Although this model works theoretically, melt mobility in migmatites is not generally observed until melt fractions approach 30% (Ding et al., 2021), so the efficacy of separating such small volume melts twice is questionable. While our model also requires separation of small volume melts (see section 4.4), it does so only once and requires both unusually inviscid melts with disequilibrium compositions (in a bulk sense) and an identified deformation catalyst.

4.4. How much lithium resource is available – the mass balance of lithium extraction

There are many uncertainties to estimates of Himalayan Li resource, but some rough calculations illustrate the efficiency of Li resource extraction from boundary layers and the source granite volume needed to produce observed pegmatites. For example, the richest pegmatites at Pusi La and Ra Chu have ~5000 ppm Li and the largest are ~1 m thick and ~100 m long. If they are also ~100 m wide, this represents 1×10^4 m^3 of rock, or $\sim1\times10^5$ kg of Li (metal) resource per pegmatite. In comparison, if a boundary layer with an average Li concentration of 2500 ppm extends 0.5 mm adjacent to a crystal (Fig. 6A), and the crystal and liquid together scale to 10 mm, the boundary layer represents ~5 vol% of the combined melt plus crystal system. If the scale of crystal plus melt is smaller, the percentage is higher (e.g., 10 vol%, if crystal plus melt scale to 5 mm). For the more conservative 5 vol% case, if quartz and feldspar constitute 70% of the rock, Li-enriched boundary layers represent ~3.5 vol% of the rock. Noting that the average concentration of Li in the modeled boundary layer is typically only about 2500 ppm (or about half the concentration in a Li-rich pegmatite), a volume of 1×10^4 m^3 of Li-enriched pegmatite requires $\sim6\times10^5$ m^3 of source rock. That is, the volume of the source rock must exceed the volume of the pegmatite by a factor of ~60. In this region of the Himalaya, the hypothesized source complexes of granites and leucogranites have km-scale thicknesses and extend for tens of km's (e.g., Searle et al., 2010). These volumes exceed the largest pegmatites by a factor of $\sim10^7$ so could, in principle, source more than 100,000 of the largest pegmatites. By comparison, repeated fractional crystallization and melt extraction (Wu et al., 2020) would require ~16,000 times more source magma than the final pegmatite. Although this volume of magma might potentially be available, the boundary layer model is several hundred times more effective at extracting Li-enriched liquids.

4.5. What happens to unextracted Li-rich melts?

Lithium-enriched melts are unlikely to be extracted 100% efficiently, so should we not observe Li-rich minerals in the source granite, e.g., along veinlets? Quite probably not. Diffusion of Li and H_2O is sufficiently fast that these melts could readily rehomogenize with residual melt to produce compositionally normal magmas. It is important that this homogenization would occur via diffusion, not mixing, as some melts are too viscous to mobilize physically. Baker (2008) documented such diffusional rehomogenization of boundary layers experimentally. Extracted lithium-enriched melts could distribute Li into the adjacent host rocks rather than coalescing to form pegmatites, leaving behind Li-poor bodies. We do sometimes observe both holmquistite and hydrothermal petalite in adjacent calc-silicate rocks.

4.6. Broader implications for pegmatite formation and compositional gaps

The conditions of our model generally characterize the ~2200 km-long STDS, so Li-pegmatite resources are likely widespread along it. Economic exploration of the STDS, not only in China but also in India, Nepal, and Bhutan, may help address future global needs for Li. Although we do not assume that our model explains every Li pegmatite, several other localities worldwide also share associations of Li pegmatites with coeval granites (*sensu lato*) and shear zones (Černý, 1991). Specific examples include the Tin–Spodumene Belt in North and South Carolina (Swanson, 2012), the Leinster pegmatites in Ireland (Barros and Menuge, 2016), the Red Cross Lake pegmatites in Manitoba (Černý et al., 2012), the Greenbushes pegmatite in western Australia (Partington, 1990), and the Tanco pegmatite in Manitoba (Kremer, 2010). Barros and Menuge (2016) show that the chemistry of the Leinster pegmatites cannot be directly derived by batch or Rayleigh crystallization of the coeval granites and granodiorites of the Leinster Batholith. However, such models assume that magmas are homogeneous with respect to fractionating liquids. If, as we argue, liquids adjacent to anhydrous minerals are more mobile, a simple geochemical link between the bulk granite and pegmatites may not be possible. For example, depletions in Zr, Y, and Ti in the Leinster pegmatites could indicate preferential segregation of water-rich boundary layers that form adjacent to anhydrous zircon, monazite, and oxides.

The absence of a Eu-anomaly in the studied Li-pegmatites raises questions of the role of feldspar in fractionating liquid. Our models are highly simplified and focus exclusively on the enrichment of Li and H_2O adjacent to anhydrous minerals without consideration of other elements and their influence on extractability. In reality, each boundary layer will be compositionally distinct, which affects its viscosity. For example, crystallization of quartz could deplete the boundary layer in SiO_2, decreasing viscosity, while crystallization of accessory minerals like oxides and phosphates probably have little effect on major element chemistry and viscosity. Although feldspar takes up high concentrations of SiO_2, the boundary layer may yet increase in SiO_2 content and decrease in Na_2O and K_2O, increasing viscosity and making boundary layers adjacent to feldspar less mobile (similar changes in chemistry adjacent to micas would further increase their boundary layer viscosities). Thus, the extractable boundary layers might not represent equilibration with feldspar and might not develop a Eu-anomaly. Modeling each mineralogically-distinct boundary layer awaits future, more detailed analysis.

More generally, differences in boundary layer compositions and mobility point to a new mechanism for chemically fractionating melts. Fractional crystallization for bulk melt applies only when crystallization rates are slow or magmas convect. Once lock-up occurs, boundary layers can form with differing water contents and viscosities. Differential mobilization of H_2O-rich layers adjacent to anhydrous minerals implies evolved melts may not reflect bulk fractional crystallization, but rather fractional crystallization of anhydrous minerals only. In the Himalaya, crystallization of anhydrous monazite, zircon, oxides, and quartz (and feldspar?) plausibly led to compositional gaps with depletions in REE, Sr, Zr, and transition metals and dramatic increases in Be, Li, Rb, and Cs. In addition to explaining the formation of Li pegmatites, this process may explain compositional gaps in magmas series more generally.

CRediT authorship contribution statement

Xiao-Chi Liu: Conceptualization, Methodology, Investigation, Visualization, Funding acquisition, Writing – original draft, Writing –

review & editing. **Matthew J. Kohn:** Writing – review & editing, Writing – original draft, Visualization, Methodology, Investigation, Funding acquisition, Conceptualization. **Jia-Min Wang:** Methodology, Investigation. **Shao-Xiong He:** Methodology, Investigation. **Ru-Cheng Wang:** Writing – review & editing, Conceptualization. **Fu-Yuan Wu:** Writing – review & editing, Visualization, Investigation, Funding acquisition, Conceptualization.

Declaration of competing interest

The authors declare that they have no known competing financial interests or personal relationships that could have appeared to influence the work reported in this paper.

Data availability

Data will be made available on request.

Acknowledgments

This work was financially supported by the Strategic Priority Research Program of the Chinese Academy of Sciences (XDA0430101), the second comprehensive scientific investigation into Qinghai–Tibet Plateau (2019QZKK0802), the National Natural Science Foundation of China (41888101), the US National Science Foundation (OIA1545903 and EAR2118114), and a fellowship from the Chinese Academy of Sciences (2020DC0024). The reviews of Mona Sirbescu and of an anonymous reviewer, as well as the careful editorial handling of Rosemary Hickey-Vargas, greatly helped us to clarify the manuscript.

Supplementary materials

Supplementary material associated with this article can be found, in the online version, at doi:10.1016/j.epsl.2024.118598.

References

Albarede, F., Bottinga, Y., 1972. Kinetic disequilibrium in trace element partitioning between phenocrysts and host lava. Geochimica et Cosmochimica Acta 36, 141–156.

Ambrose, H., Kendall, A., 2020. Understanding the future of lithium: Part 1, resource model 24 (1), 80–89.

Bachmann, O., Bergantz, G., 2008. The magma reservoirs that feed supereruptions. Elements 4, 17–21.

Baker, D.R., Freda, C., Brooker, R.A., Scarlato, P., 2005. Volatile diffusion in silicate melts and its effects on melt inclusions. Annals of Geophysics 48, 699–717.

Baker, D.R., 2008. The fidelity of melt inclusions as records of melt composition. Contributions to Mineralogy and Petrology 156, 377–395.

Barros, R., Menuge, J.F., 2016. The origin of spodumene pegmatites associated with the Leinster Granite in southeast Ireland. The Canadian Mineralogist 54, 847–862.

Bottinga, Y., 1970. Densities of liquid silicate systems calculated from parital molar volumes of oxide components. American Journal of Science 269, 169–182.

Bowers, T.S., Helgeson, H.C., 1983. Calculation of the thermodynamic and geochemical consequences of nonideal mixing in the system H_2O-CO_2 -NaCl on phase relations in geologic systems; metamorphic equilibria at high pressures and temperatures. American Mineralogist 68, 1059–1075.

Brenan, J.M., Neroda, E., Lundstrom, C.C., Shaw, H.F., Ryerson, F.J., Phinney, D.L., 1998. Behaviour of boron, beryllium, and lithium during melting and crystallization: constraints from mineral-melt partitioning experiments. Geochimica et Cosmochimica Acta 62, 2129–2141.

Burchfiel, B.C., Chen, Z.L., Hodges, K.V., Liu, Y.P., Royden, L.H., Deng, C.R., Xu, J.N., 1992. The South Tibetan Detachment System, Himalayan Orogen: Extension contemporaneous with and parallel to shortening in a collisional mountain belt. Geological Society of America Special Papers 269, 1–41.

Černý, P., 1991. Rare-element granitic pegmatites. Part II: regional to global environments and petrogenesis. Geoscience Canada 18, 68–81.

Černý, P., Teertstra, D.K., Chapman, R., Selway, J.B., Hawthorne, F.C., Ferreira, K., Chackowsky, L.E., Wang, X.-J., Meintzer, R.E., 2012. Extreme fractionation and deformation of the leucogranite – Pegmatite suite at Red Cross lake, Manitoba, Canada. IV. Mineralogy. The Canadian Mineralogist 50, 1839–1875.

Cottle, J.M., Waters, D.J., Riley, D., Beyssac, O., Jessup, M.J., 2011. Metamorphic history of the South Tibetan Detachment System, Mt. Everest region, revealed by RSCM thermometry and phase equilibria modelling. Journal of Metamorphic Geology 29, 561–582.

Dahlen, F., 1990. Critical taper model of fold-and-thrust belts and accretionary wedges. Annual Review of Earth and Planetary Sciences 18, 55–99.

Ding, H., Kohn, M.J., Zhang, Z., 2021. Long-lived (ca. 22–24 Myr) partial melts in the eastern Himalaya: Petrochronologic constraints and tectonic implications. Earth and Planetary Science Letters 558, 116764.

Ellis, B.S., Neukampf, J., Bachmann, O., Harris, C., Forni, F., Magna, T., Laurent, O., Ulmer, P., 2022. Biotite as a recorder of an exsolved Li-rich volatile phase in upper-crustal silicic magma reservoirs. Geology 50, 481–485.

Fan, J.-J., Tang, G.-J., Wei, G.-J., Wang, H., Xu, Y.-G., Wang, Q., Zhou, J.-S., Zhang, Z.-Y., Huang, T.-Y., Wang, Z.-L., 2020. Lithium isotope fractionation during fluid exsolution: Implications for Li mineralization of the Bailongshan pegmatites in the West Kunlun. NW Tibet. Lithos 352-353, 105236.

Fenn, P.M., 1986. On the origin of graphic granite. American Mineralogist 71, 325–330.

Giordano, D., Russell, J.K., Dingwell, D.B., 2008. Viscosity of magmatic liquids: A model. Earth and Planetary Science Letters 271, 123–134.

Grew, E.S., 1998. Boron and beryllium minerals in granulite-facies pegmatites and implications of beryllium pegmatites for the origin and evolution of the Archean Napier Complex of east Antarctica. Memoirs of National Institute of Polar Research. Special issue 53, 74–92.

Hacker, B.R., Abers, G.A., 2004. Subduction Factory 3: An Excel worksheet and macro for calculating the densities, seismic wave speeds, and H_2O contents of minerals and rocks at pressure and temperature. Geochemistry, Geophysics, Geosystems 5.

Hess, K.-U., Dingweil, D., Webb, S., 1995. The influence of excess alkalis on the viscosity of a haplogranitic melt. American Mineralogist 80, 297–304.

Hess, K., Dingwell, D.B., 1996. Viscosities of hydrous leucogranitic melts: A non-Arrhenian model. American Mineralogist 81, 1297–1300.

Holtz, F., Johannes, W., Tamic, N., Behrens, H., 2001. Maximum and minimum water contents of granitic melts generated in the crust: a reevaluation and implications. Lithos 56, 1–14.

Icenhower, London, David, J., 1995. An experimental study of element partitioning among biotite, muscovite, and coexisting peraluminous silicic melt at 200 MPa (H_2O). American Mineralogist 80, 1229–1251.

Jahns, R.H., 1982. Internal evolution of pegmatite bodies. In: Černý, P. (Ed.), Granitic pegmatites in science and industry, 8. Mineralogical Association of Canada Short Course Handbook, pp. 293–327.

Jessup, M.J., Cottle, J.M., 2010. Progression from south-directed extrusion to orogen-parallel extension in the southern margin of the Tibetan Plateau, Mount Everest region. Tibet. The Journal of Geology 118, 467–486.

Jolliff, B.L., Papike, J.J., Shearer, C.K., 1992. Petrogenetic relationships between pegmatite and granite based on geochemistry of muscovite in pegmatite wall zones, Black Hills, South Dakota, USA. Geochimica et Cosmochimica Acta 56, 1915–1939.

Kesler, S.E., Gruber, P.W., Medina, P.A., Keoleian, G.A., Everson, M.P., Wallington, T.J., 2012. Global lithium resources: Relative importance of pegmatite, brine and other deposits. Ore Geology Reviews 48, 55–69.

Kohn, M.J., 2014. Himalayan metamorphism and its tectonic implications. Annual Review of Earth and Planetary Sciences 42, 381–419.

Kohn, M.J., Penniston-Dorland, S.C., 2017. Diffusion: Obstacles and opportunities in petrochronology. Reviews in Mineralogy and Geochemistry 83, 103–152.

Koopmans, L., Martins, T., Linnen, R., Gardiner, N.J., Breasley, C.M., Palin, R.M., Groat, L.A., Silva, D., Robb, L.J., 2023. The formation of lithium-rich pegmatites through multi-stage melting. Geology. Inpress.

Kremer, P., 2010. Structural geology and geochronology of the Bernic Lake area in the Bird River greenstone belt, Manitoba: evidence for syn-deformational emplacement of the Bernic Lake pegmatite group. University of Waterloo.

Kress, V.C., Carmichael, I.S., 1991. The compressibility of silicate liquids containing Fe_2O_3 and the effect of composition, temperature, oxygen fugacity and pressure on their redox states. Contributions to Mineralogy and Petrology 108, 82–92.

Lange, R.A., 1994. The effect of H_2O, CO_2 and F on the density and viscosity of silicate melts. Reviews in Mineralogy and Geochemistry 30, 331–369.

Lange, R.A., Carmichael, I.S.E., 1987. Densities of Na_2O-K_2O-CaO-MgO-FeO-Fe_2O_3-Al_2O_3-TiO_2-SiO_2 liquids: New measurements and derived partial molar properties. Geochimica et Cosmochimica Acta 51, 2931–2946.

Law, R.D., Jessup, M.J., Searle, M.P., Francsis, M.K., Waters, D.J., Cottle, J.M., 2011. Telescoping of isotherms beneath the South Tibetan Detachment System. Mount Everest Massif. J. Struct. Geol. 33, 1569–1594.

Liu, C., Wang, R.-C., Wu, F.-Y., Xie, L., Liu, X.-C., Li, X.-K., Yang, L., Li, X.-J., 2020. Spodumene pegmatites from the Pusila pluton in the higher Himalaya, South Tibet: Lithium mineralization in a highly fractionated leucogranite batholith. Lithos 358-359, 105421.

London, D., Morgan, G.B., Hervig, R.L., 1989. Vapor-undersaturated experiments with Macusani glass+ H2O at 200 MPa, and the internal differentiation of granitic pegmatites. Contributions to Mineralogy and Petrology 102, 1–17.

London, D., 1992. The application of experimental petrology to the genesis and crystallization of granitic pegmatites. The Canadian Mineralogist 30, 499–540.

London, D., 2014. A petrologic assessment of internal zonation in granitic pegmatites. Lithos 184-187, 74–104.

Maloney, J.S., Nabelek, P.I., Sirbescu, M.-L.C., Halama, R., 2008. Lithium and its isotopes in tourmaline as indicators of the crystallization process in the San Diego County pegmatites, California, USA. European Journal of Mineralogy 20, 905–916.

Maneta, V., Baker, D.R., 2014. Exploring the effect of lithium on pegmatitic textures: An experimental study. American Mineralogist 99, 1383–1403.

McKenzie, D., 1985. The extraction of magma from the crust and mantle. Earth and Planetary Science Letters 74, 81–91.

Partington, G.A., 1990. Environment and structural controls on the intrusion of the giant rare metal Greenbushes Pegmatite. Western Australia. Economic Geology 85, 437–456.

Phelps, P.R., Lee, C.-T.A., Morton, D.M., 2020. Episodes of fast crystal growth in pegmatites. Nature communications 11, 1–10.

Qin, K., Zhao, J., He, C., Shi, R., 2021. Discovery of the Qongjiagang giant lithium pegmatite deposit in Himalaya, Tibet, China. Acta Petrologica Sinica 37, 3277–3286.

Rockhold, J.R., Nabelek, P.I., Glascock, M.D., 1987. Origin of rhythmic layering in the Calamity Peak satellite pluton of the Harney Peak Granite, South Dakota: The role of boron. Geochimica et Cosmochimica Acta 51, 487–496.

Rubin, A.M., 1995. Propagation of magma-filled cracks. Annual Review of Earth and Planetary Sciences 23, 287–336.

Rudnick, R.L., Gao, S., 2014. Composition of the Continental Crust. In: Holland, H.D., Turekian, K.K. (Eds.), Treatise on Geochemistry, Second Edition. Elsevier, Oxford, pp. 1–51.

Rutter, E., Neumann, D., 1995. Experimental deformation of partially molten Westerly granite under fluid-absent conditions, with implications for the extraction of granitic magmas. Journal of Geophysical Research: Solid Earth 100, 15697–15715.

Scaillet, B., Searle, M.P., 2006. Mechanisms and timescales of felsic magma segregation, ascent and emplacement in the Himalaya. Geological Society, Special Publications 268, 293–308.

Searle, M.P., Cottle, J.M., Streule, M.J., Waters, D.J., 2009. Crustal melt granites and migmatites along the Himalaya: melt source, segregation, transport and granite emplacement mechanisms. Earth and Environmental Science Transactions of the Royal Society of Edinburgh 100, 219–233.

Sirbescu, M.-L.C., Hartwick, E.E., Student, J.J., 2008. Rapid crystallization of the Animikie Red Ace Pegmatite, Florence county, northeastern Wisconsin: inclusion microthermometry and conductive-cooling modeling. Contributions to Mineralogy and Petrology 156, 289–305.

Sirbescu, M.-L.C., Schmidt, C., Veksler, I.V., Whittington, A.G., Wilke, M., 2017. Experimental crystallization of undercooled felsic liquids: Generation of pegmatitic texture. Journal of Petrology 58, 539–568.

Swanson, S.E., 2012. Mineralogy of spodumene pegmatites and related rocks in the tin–spodumene belt of north Carolina and south Carolina, USA. The Canadian Mineralogist 50, 1589–1608.

Tiller, W.A., Jackson, K.A., Rutter, J.W., Chalmers, B., 1953. The redistribution of solute atoms during the solidification of metals. Acta Metallurgica 1, 428–437.

Webber, K.L., Simmons, W.B., Falster, A.U., Foord, E.E., 1999. Cooling rates and crystallization dynamics of shallow level pegmatite-aplite dikes, San Diego County, California. American Mineralogist 84, 708–717.

Webster, J., Holloway, J., Hervig, R., 1989. Partitioning of lithophile trace elements between H_2O and H_2O+CO_2 fluids and topaz rhyolite melt. Economic Geology 84, 116–134.

Weinberg, R.F., 2016. Himalayan leucogranites and migmatites: nature, timing and duration of anatexis. Journal of Metamorphic Geology 34, 821–843.

Wu, F.-Y., Liu, X.-C., Liu, Z.-C., Wang, R.-C., Xie, L., Wang, J.-M., Ji, W.-Q., Yang, L., Liu, C., Khanal, G.P., 2020. Highly fractionated Himalayan leucogranites and associated rare-metal mineralization. Lithos 352, 105319.

Yin, A., 2006. Cenozoic tectonic evolution of the Himalayan orogen as constrained by along-strike variation of structural geometry, exhumation history, and foreland sedimentation. Earth-Science Reviews 76, 1–131.

Zajacz, Z., Halter, W.E., Pettke, T., Guillong, M., 2008. Determination of fluid/melt partition coefficients by LA-ICPMS analysis of co-existing fluid and silicate melt inclusions: controls on element partitioning. Geochimica et Cosmochimica Acta 72, 2169–2197.

Zajacz, Z., Hanley, J.J., Heinrich, C.A., Halter, W.E., Guillong, M., 2009. Diffusive reequilibration of quartz-hosted silicate melt and fluid inclusions: are all metal concentrations unmodified? Geochimica et Cosmochimica Acta 73, 3013–3027.

Zhang, J., Lee, C.-T.A., 2021. Disequilibrium crystallization and rapid crystal growth: A case study of orbicular granitoids of magmatic origin. International Geology Review 63, 900–916.

Zhang, Y., Ni, H., 2010. Diffusion of H, C, and O components in silicate melts. Reviews in Mineralogy and Geochemistry 72, 171–225.

Zhang, Y., Ni, H., Chen, Y., 2010. Diffusion data in silicate melts. Reviews in Mineralogy and Geochemistry 72, 311–408.